INTERNAL COMPUTATIONAL FLUID MECHANICS ON SUPERCOMPUTERS FOR AEROSPACE PROPULSION SYSTEMS

Bernhard H. Anderson
Thomas J. Benson
NASA Lewis Research Center

SUMMARY

The accurate calculation of three-dimensional internal flowfields for application towards aerospace propulsion systems requires computational resources available only on supercomputers. This paper presents a survey of three-dimensional calculations of hypersonic, transonic and subsonic internal flowfields conducted at the Lewis Research Center. A steady state PNS solution of flow in a Mach 5.0 mixed compression inlet, a Navier-Stokes solution of flow in the vicinity of a terminal shock, and a PNS solution of flow in a diffusing S-bend with vortex generators will be presented and discussed. All of these calculations have been performed on either the NAS Cray 2 or the Lewis Research Center's Cray XMP.

INTRODUCTION

The accurate calculation of three-dimensional internal flowfields for application towards aerospace propulsion systems requires computational resources available only on supercomputers. Aerospace flowfields in physically realistic situations are strongly three-dimensional and viscous (as well as usually turbulent) and contain strong shock wave interactions. It is also important to predict and validate the relevant flow physics which may require large numbers of grid points. The geometry associated with aerospace and/or special performance aircraft inlets and nozzles are highly complex. These ducts typically contain large area variations, highly curved or offset centerlines, and various flow control devices including boundary layer bleed or blowing slots or vortex generators. A detailed description of these geometric features requires very fine grid systems while the flow within these geometries requires an even finer grid. Boundary layers which must be computationally resolved are generated on all internal surfaces. Strong secondary flows which are often generated in the ducts must also be resolved. If the flow is supersonic one must also accurately compute shock wave strength and location, the interaction of multiple shock waves, and the interaction of the shock waves with boundary layers within the duct. To computationally resolve all of these phenomena requires extremely fine grid systems with the accompanying large computer storage and execution time requirements.

Computer code modelling of internal flows has increased recently due to improved computer algorithms and more powerful supercomputers such as the Cray-XMP and Cray 2. Some researchers, Refs (1 to 3), have used the unsteady Reynolds-averaged Navier-Stokes (NS) equations marched in time to a steady state solution to describe the flow in the duct. At NASA Lewis, ducts have been analyzed with a zonal methodology, Ref (4); NS codes are used only in the transonic terminal shock region, while higher speed Parabolized Navier-Stokes (PNS) codes are used in the hypersonic and subsonic diffusers. Through an extensive code verification effort, Ref (4), it has been found that the higher computational speed of the PNS codes provides the analyst sufficient grid resolution to resolve critical flow phenomenon and that lack of sufficient grid resolution often leads to erroneous results. However, these codes have their limitations; they typically cannot calculate through transonic regions of mixed supersonic and subsonic flows, and they cannot properly model regions with large recirculations. Because such flow phenomenon are present near strong normal shock waves, NS codes are used in these cases.

This report will survey the results from three studies using supercomputers at the NASA Lewis Research Center on internal computational fluid mechanics which are typical of aerospace propulsion systems. Details of two of the computations can be found in the literature, Refs (5 and 6), while the third is originally presented here. The first case involves the three-dimensional calculation of hypersonic flow in a Mach 5.0 mixed compression inlet, Ref (5), which will be tested in the Lewis 10x10 foot supersonic wind tunnel. The results of the analysis are compared with preliminary experimental results. In the second case, the two-dimensional Navier-Stokes calculations of a Mach 1.3 and Mach 1.6 normal shock/boundary layer interaction in a rectangular wind tunnel is studied. The results of the analysis are compared with LDV experimental results obtained in the Lewis 1x1 supersonic wind tunnel. The third case involves the three-dimensional subsonic calculation of flow in a diffusing S-bend duct, Ref (6), with vortex generators. The results of the analysis are compared with experimental results from the University of Tennessee, Ref (7).

RESULTS

3D Hypersonic Inlet

The Mach 5.0 hypersonic mixed compression to be analyzed is shown in Figure (1). This inlet has rectangular cross-section, a pre-compression ramp and three compression ramps external to the cowl. A shock is generated on the pre-compression ramp when the aircraft is at angle of attack. This shock and the shocks from the ramps are designed to fall just outside the cowl lip at the design Mach number. The cowl lip generates a shock which is cancelled at the ramp shoulder and the cowl is contoured to further compress the flow internally. A swept sideplate runs from the leading edge of the pre-compression plate to the

leading edge of the cowl to minimize the drag generated by compressed flow spilling over the sides of the inlet.

The Mach 5.0 inlet has been analyzed three-dimensionally using a PNS analysis program. The free stream Mach number was 5.0, angle of attack was 9.0 degrees and Reynolds number per foot was 2500000. The computations were performed on an 80x60 cross-sectional grid, which corresponds to the levels of grid resolution required for accurate modelling of the glancing shock/boundary layer interaction (GSBLI), Ref (4), and were marched 630 stations from free stream to near the inlet throat. The calculation required nearly three million mesh points and slightly less than two hours cpu time on the Cray 2.

The results from the three-dimensional calculation are presented in a series of figures (2 to 9). At the top of each figure is a schematic of the inlet, with the location of the cross-sectional plane given by a vertical line and a prescribed distance from the inlet leading edge. The bottom of the figure shows the flowfield in a cross-section of the inlet; the ramp surface is at the bottom, the cowl surface at the top, and sideplates are on both sides. Because of flow symmetry, only half of the inlet was calculated. The left side of the figure shows Mach number contours, while the right side shows secondary velocity within the cross-sectional plane. The figures proceed from a location just downstream from the inlet leading edge to a location inside the cowl near the throat. On the solid surface of the ramp, cowl and sideplate, one will note the development and growth of the boundary layer by a concentration of Mach contours near these surfaces. Shock waves are noted by a concentration of Mach contours away from the solid surfaces. They can also be detected by an abrupt change in the secondary velocity vectors. In this calculation, the compression shocks and the Mach contours are parallel to the ramp and cowl surfaces.

Initially, Figure (2), the incoming flow is uniform at Mach 5.0 and 9.0 degrees angle of attack. The velocity vectors point down because the flow is at angle of attack. A shock generated by the pre-compression ramp appears as a horizontal line in the Mach contours. At the initial station, no boundary layers are noted and there are no sideplates present. As one proceeds downstream to the first ramp, Figure (3), the boundary layer has grown uniformly on the ramp surface and is thicker near the ramp than near the edge of the sideplate, as shown in the Mach contours. The non-uniformity of the sideplate boundary layer is due to the cut-back leading edge of the plate; the lower portion of the sideplate has a longer run than the upper and has therefore a thicker boundary layer. The shock from the pre-compression ramp lies just near the edge of the sideplate.

Entering the region of the compression ramps, Figure (4) shows the flowfield just downstream of the first ramp. The shock generated by this ramp is evident in the Mach contours; near the center of the flowfield this shock is flat while near the sideplate the shock forms a characteristic lamda as it interacts with the boundary layer of the sideplate. In the secondary velocity vectors, one sees a cross-flow being induced along the sideplate and feeding forward of the inviscid shock location; flow conditions which have previously been found in the GSBLI calculations. Each of the succeeding compression ramps generates another GSBLI along the sideplate which increases the secondary flow, as shown in Figure (5). A circulation region has been generated near the sideplate corner, pulling in flow along the ramp surface.

Near the cowl lip, the flow field appears as Figure (6). The secondary velocity vectors show extremely strong flow along the sideplate, while the Mach number contours show the sideplate boundary layer to be highly distorted. The boundary layer has been thickened in the vicinity of the shock waves and thinned in the corner formed by the ramp and sideplate. The secondary velocity vectors also show flow being drawn along the ramp surface into this corner. The boundary layer along the ramp surface is quite thick and corresponds to the thickness predicted in the two-dimensional calculations. The strong secondary flows induced by the multiple GSBLI persist even though the shock waves have left the flow domain over the cowl. The flowfield from the inlet leading edge to the cowl lip has been shaped by the thick boundary layer that grows on the ramp and sideplate and the multiple GSBLI that occur on the sideplate due to the compression ramps. The flow is highly three-dimensional at the cowl lip with low energy boundary layer flow being swept up along the sideplate.

As the flow enters the cowl, Figure (7) shows that a shock wave is generated by the cowl lip. This shock, indicated by the horizontal lines in the Mach contours, moves down through the flow field as shown in Figures (8 and 9). The strong secondary flow moving up the sideplate encounters the internal cowl surface and the secondary velocity vectors indicate that this flow turns through the corner formed by the cowl and sideplate. Figures (8 and 9) show that two things happen as the secondary flow turns this corner; first, the secondary flow rolls up into a vortex, and second, the low energy flow is concentrated in the corner. The internal surface of the cowl has been shaped to further compress the flow. As the low energy flow in the corner is subjected to the adverse pressure gradient created by this turning, a large separation occurs.

The last calculated cross-section is shown in Figure (9). The shock from the cowl is about to hit the ramp surface, while the large separation region exists in the corner. The secondary flow has rolled into a vortex near the sideplate, while along the ramp flow continues into the corner. Figure (10) shows another view of the ramp flow near the inlet cowl. This figure shows oil flow results from a subscale model of the inlet which was tested at NASA Lewis. The oil flow indicates that the flow near the ramp surface is drawn in towards the sideplate. This figure shows velocity vectors on the surface of the ramp from the third ramp to the cowl. In the lower left corner of the figure the computed velocity vectors near the ramp surface are shown. The velocity vectors also indicate that flow is drawn in toward the sideplate because of the GSBLI. This is the first

qualitative verification of the results of the Mach 5.0 inlet study.

Normal Shock Wave Turbulent Boundary Layer Interaction

As part of a continuing code verification effort at NASA Lewis, the three-dimensional normal shock/boundary layer interaction is being studied both analytically and experimentally. In this study, a normal shock is formed in the constant area, square cross section, test section of a wind tunnel with free stream Mach numbers of 1.3 and 1.6. The normal shock interacts with the boundary layers that have grown on the tunnel walls; the pressure rise across the shock is felt upstream through the subsonic part of the boundary layer, the boundary layer thickens and in some cases separates from the wall. The normal shock in the vicinity of the wall is lamda shaped, with the flow passing through two oblique shocks instead of the single normal shock. In some cases, this can produce a supersonic tongue region downstream of the normal shock and near the tunnel wall. The thickening of the boundary layer can also cause reacceleration of the flow to supersonic conditions and formation of multiple normal shocks.

Because of the mixed supersonic/subsonic nature of the flowfield in the normal shock/ boundary layer interaction, and because of the possible large recirculation region, a full Navier-Stokes calculation of this flowfield is required. In the present study, a time dependent linearized block implicit scheme has been time marched to a steady state solution of the normal shock/boundary layer interaction problem. In the preliminary stages of the study, the calculations have been performed two-dimensionally on 30x60 grids, on the Lewis Cray-XMP. These studies will be extended to much finer grids and three dimensions on the Cray 2. Two cases have been run; one at Mach number 1.3 and the other at Mach number 1.6. In both cases the initial conditions were uniform free stream flow with a turbulent boundary layer profile near the wall equal in thickness to the measured experimental upstream thickness. The incoming conditions were then held fixed, while the downstream pressure was set equal to the normal shock static pressure rise. This caused a normal shock to be formed near the exit of the computed flowfield. This shock moved upstream, interacting with the boundary layer on the wall until it finally stabilized near the middle of the computational flowfield. No slip boundary conditions were applied along the wall, symmetry conditions along the upper boundary, and extrapolation conditions, except for pressure, along the exit. The solution was time marched until the magnitude of the residuals was less than 10-04.

The results of the calculations are compared to experimental results in Figures (11 and 12). Figure (11) shows Mach number contours for free stream Mach number 1.3. The calculated results are shown in the upper half of the figure, while the lower half shows experimental LDV results. The shock location is noted by the vertical and contour lines, the flow is from left to right, and the wall boundary layers are indicated by the contour lines at the top and bottom. The comparison between calculated and experimental results is quite good; the boundary layer is seen to thicken downstream of the shock, the shock strength is correctly modelled, and the calculations correctly indicate no flow separation in the vicinity of the shock. A rather weak lamda is formed both analytically and experimentally at the foot of the normal shock. When the free stream Mach number is increased to 1.6, the flowfield appears as in Figure (12). Again the calculated two-dimensional results are in the upper half of the figure while the LDV results along the tunnel centerline are given in the lower half. Upstream of the normal shock, the comparison between analysis and experiment are quite good; the analysis correctly predicts flow separation beneath the shock and correctly predicts the shape, height and upstream extent of the lamda at the foot of the shock. Downstream of the shock, however, the experiment indicates that the flow is reaccelerated to supersonic conditions and forms an additional weak normal shock, while the analysis does not predict this behavior. Additional oil flow results from the experiment show that there are large separation regions in the corners of the test section which introduce important three-dimensional effects. These three-dimensional effects are not currently modelled in the two-dimensional analysis; it is hoped that the Cray 2 calculations will better agree with the experimental results.

Subsonic S-Bend Diffuser with Vortex Generators

The flow in a diffusing S-bend duct with vortex generators has been studied both computationally, Ref (6) and experimentally, Ref (7). Figure (13) shows a schematic drawing of the 30 degree-30 degree diffuser. The flow in this duct was turbulent with a Mach number of 0.6 and a Reynolds number based on the duct diameter of 1760400. The initial conditions were measured at 1.65 duct diameters upstream of the first bend to remove the influence of the bend on the static pressure. The initial boundary layer thickness was 0.1 times the initial duct radius and the area ratio was 1.51. Without the vortex generators present, a large flow separation is detected in the diffuser both analytically and experimentally because of the high degree of offset and shortness of the diffuser. To remove this separation, three pairs of vortex generators were placed in the duct at the location noted in the figure.

The flow in the S-bend diffuser was computed using a three-dimensional PNS analysis. The standard analysis was modified to include a model of the vortex generators which accounted for both the vorticity and drag of the devices. This model was verified for benchmark configurations before being applied to the diffusing S-duct. The computations were performed on a 50x50 cross section with 100 streamwise stations and required less than six minutes cpu time on the Lewis Cray-XMP.

Figures 14(a) and 14(b) show the computed and experimental total pressure coefficient in the S-bend for the vortex generator configuration described above. The maximum and minimum values

are shown at each streamwise station. At the theta = 15 degrees point the effect of the vortex generators is evident in the contours. The computed results compare qualitatively well with the experimental results. In both set of contours the distortion caused by the generators is pushed toward the outside of the first bend opposing the pressure driven secondary flow. Although Figures 14(a) and (b) still show a very distorted flow, the difference between the maximum and the minimum values is much less here than in the duct without vortex generators. Figures (15) and (16) show the secondary flow development at the inflection plane and at the duct exit. In the experimental results at the inflection plane, the vortex due to the pressure driven secondary flow has washed out the vortices from the vortex generators except near the inside of the first bend. The contour plot indicates that in this region there may still be some interaction between the vortex generator vortex and the one induced by the pressure difference. The computed results at the inflection point show that all of the vortices have been washed out by the pressure driven secondary flow. At the exit of the bend both the experimental and computed results indicate less secondary flow into the outside of the second bend than without the vortex generators. Also near the walls they indicate more flow back toward the inside of the second bend. The experimental results show a higher level of flow toward the outside of the bend in the core flow than do the computed results.

CONCLUSIONS

A survey of supercomputer calculations of internal flows which have application towards aerospace propulsion systems at the Lewis Research Center have been presented. These calculations require large amounts of computer storage and the high computational speeds which are currently available only on supercomputers. In each of the cases presented, supercomputer analysis was able to properly model physical phenomenon seen experimentally. The need to resolve critical interactions within aerospace propulsion systems and the desire to analyze more complex flowfields are driving the need for supercomputers.

REFERENCES

1. White, M. E., Drummond, J. P., and Kumar, A., "Evolution and Status of CFD Techniques for Scramjet Applications," AIAA Paper No. 86-0160, January 1986.

2. Knight, D. D., "Improving Numerical Simulation of High Speed Inlets Using the Navier-Stokes Equations," AIAA Paper No. 80-0383, January 1980.

3. Campbell, A. F., and Forester, C. K., "Evaluation of a Method for Analyzing the Aperture Region of Two-Dimensional External Compression Inlets," AIAA Paper No. 85-3072, October, 1985.

4. Anderson, B. H., "Three-Dimensional Viscous Design Methodology for Advanced Technology Aircraft Supersonic Inlet Systems," NASA TM 83558, January 1984.

5. Benson, T. J., "Three-Dimensional Viscous Calculation of Flow in a Mach 5.0 Hypersonic Inlet," AIAA Paper No. 86-1461, June 1986.

6. Kunik, W. G., "Application of a Computational Model for Vortex Generators in Subsonic Internal Flows," AIAA Paper No. 86-1458, June 1986.

7. Vakili, A. D., Wu, J. P., Liver, P., and Bhat, M. K., "Flow Control in a Diffusing S-Duct," AIAA Paper 85-0524, March 1985.

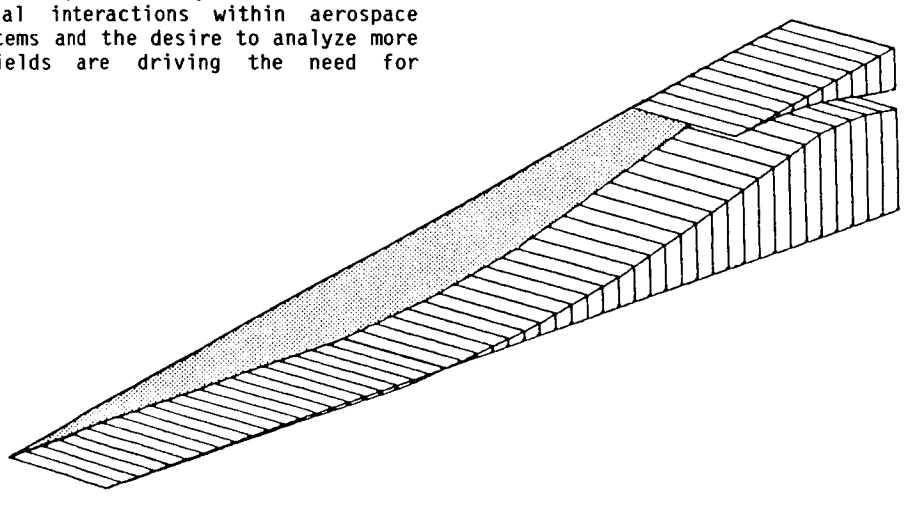

Figure 1. –Mach 5.0 hypersonic inlet geometry

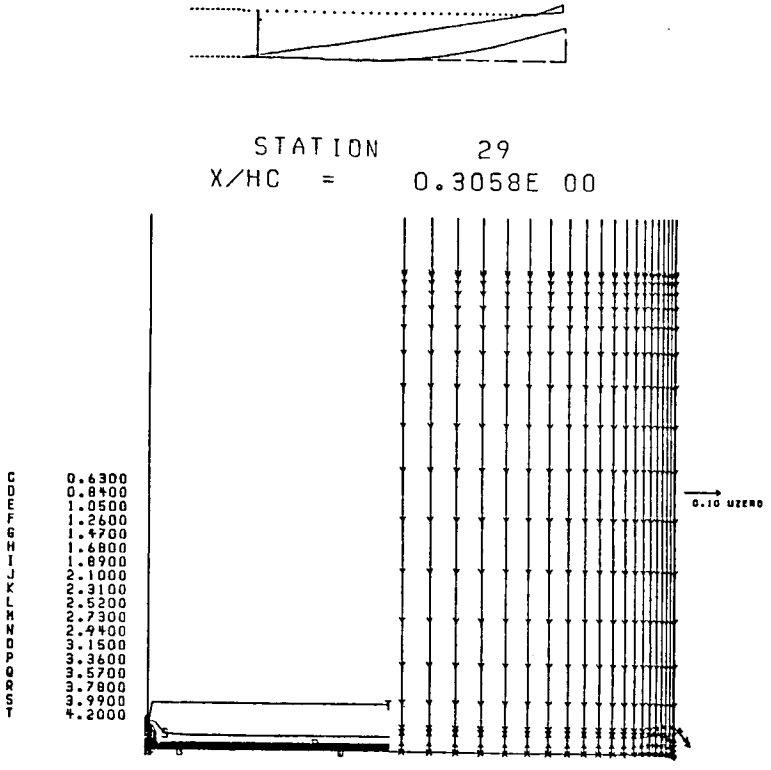

Figure 2. –Mach number contours and secondary velocity vectors on pre–compression ramp

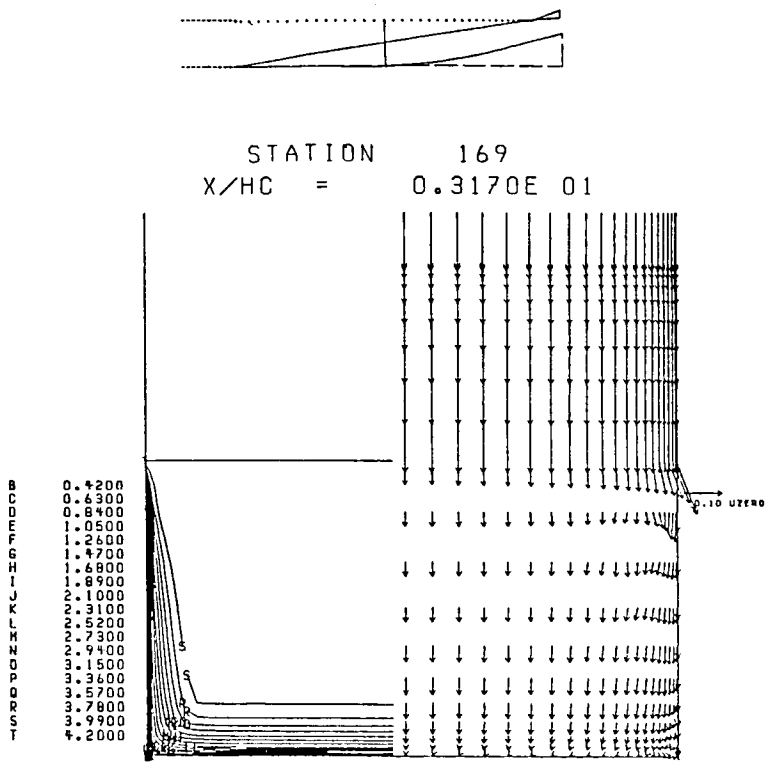

Figure 3. –Mach number contours and secondary velocity vectors before first ramp

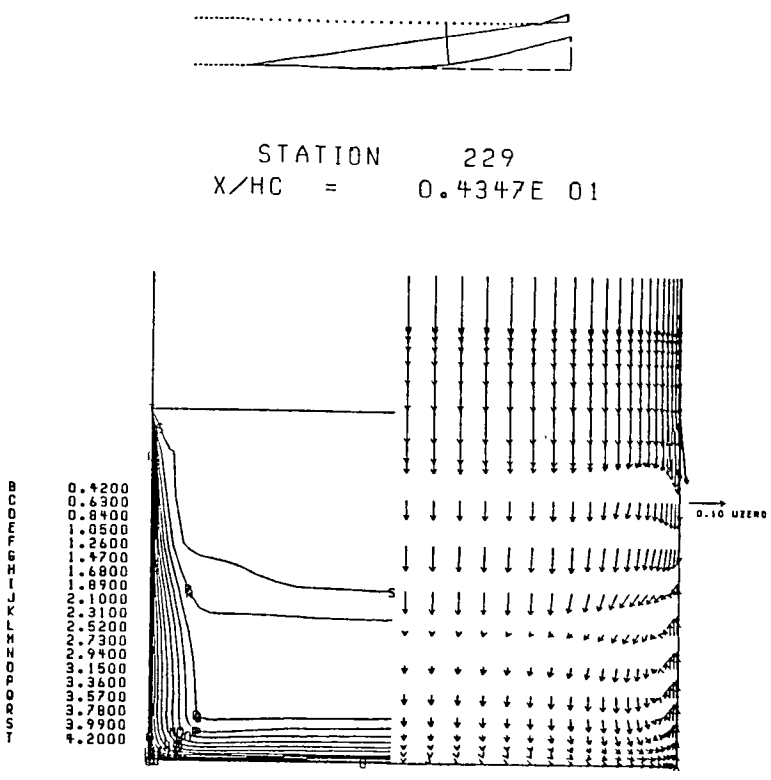

Figure 4. –Mach number contours and secondary velocity vectors aft of first ramp.

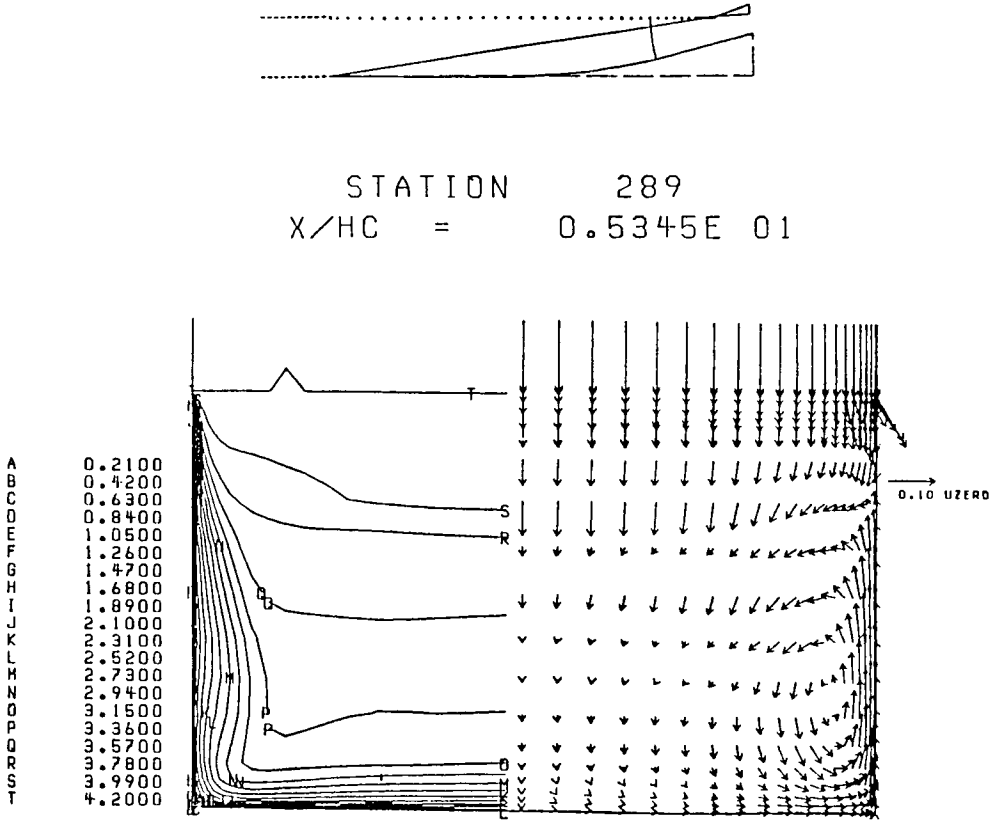

Figure 5. —Mach number contours and secondary velocity vectors aft of third ramp.

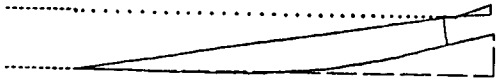

STATION 369
X/HC = 0.6158E 01

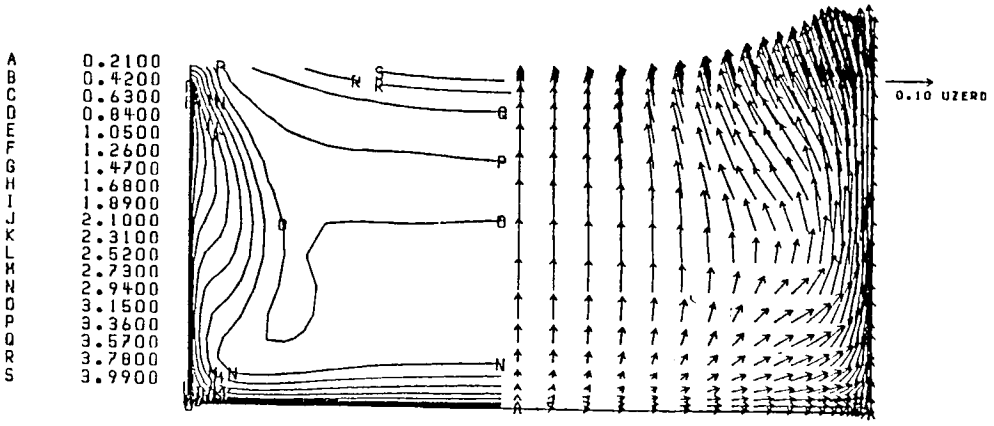

Figure 6. –Mach number contours and secondary velocity vectors before cowl lip.

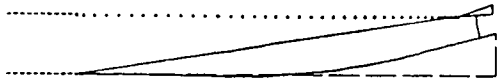

STATION 549
X/HC = 0.6655E 01

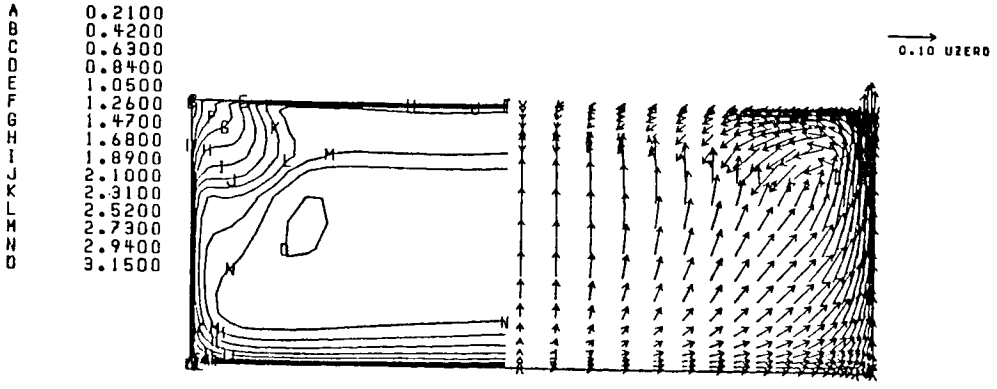

Figure 7. –Mach number contours and secondary velocity vectors aft of cowl lip.

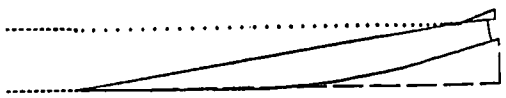

STATION 589
X/HC = 0.6802E 01

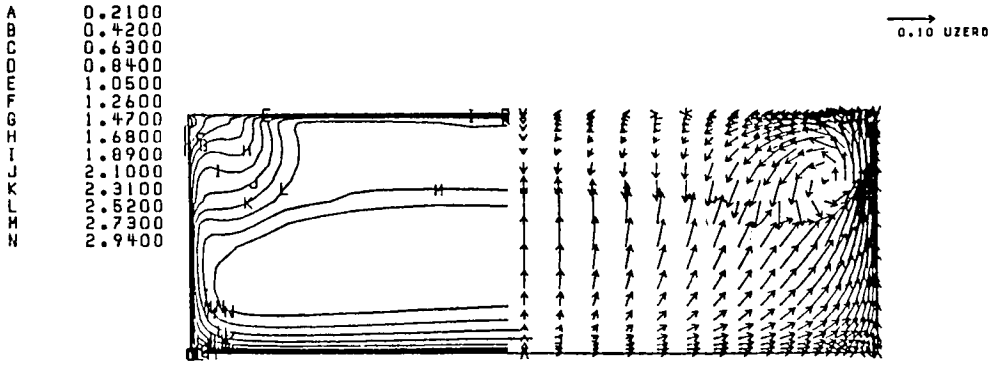

Figure 8. –Mach number contours and secondary velocity vectors for 3D inlet calculation.

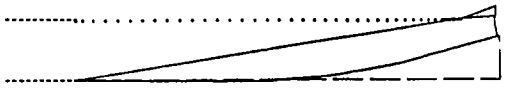

STATION 629
X/HC = 0.6887E 01

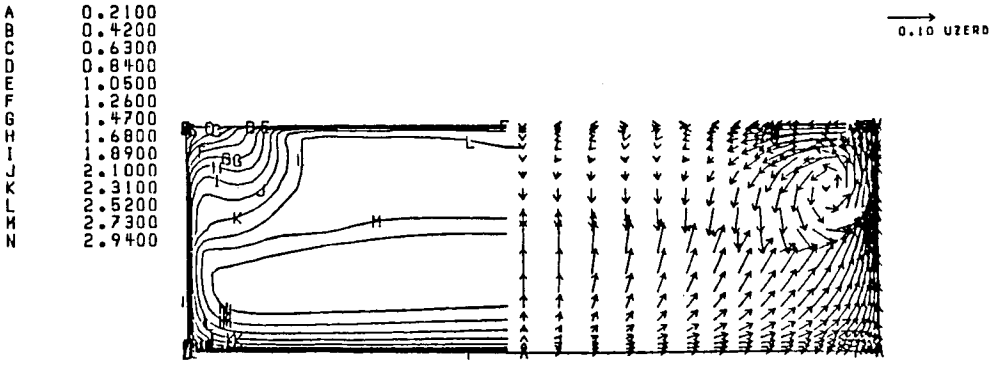

Figure 9. –Mach number contours and secondary velocity vectors at corner separation.

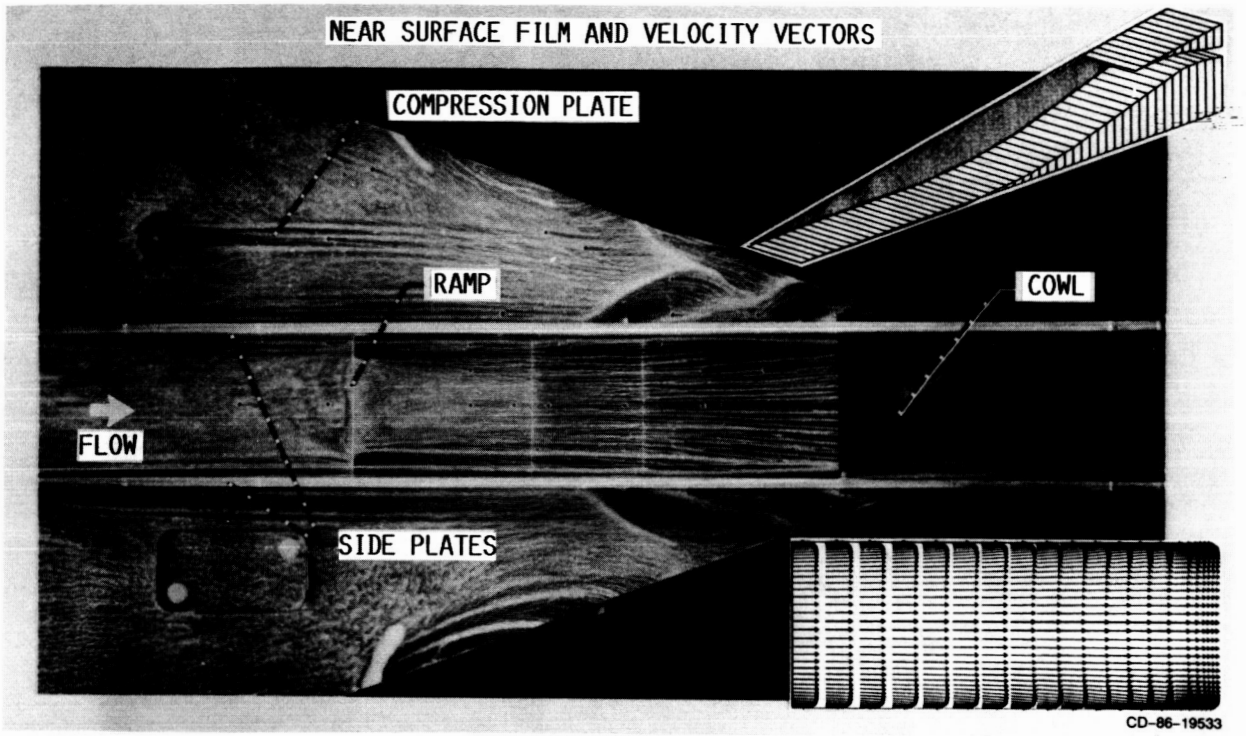

Figure 10. Surface oil flow and calculated velocity vectors for inlet ramp surface.

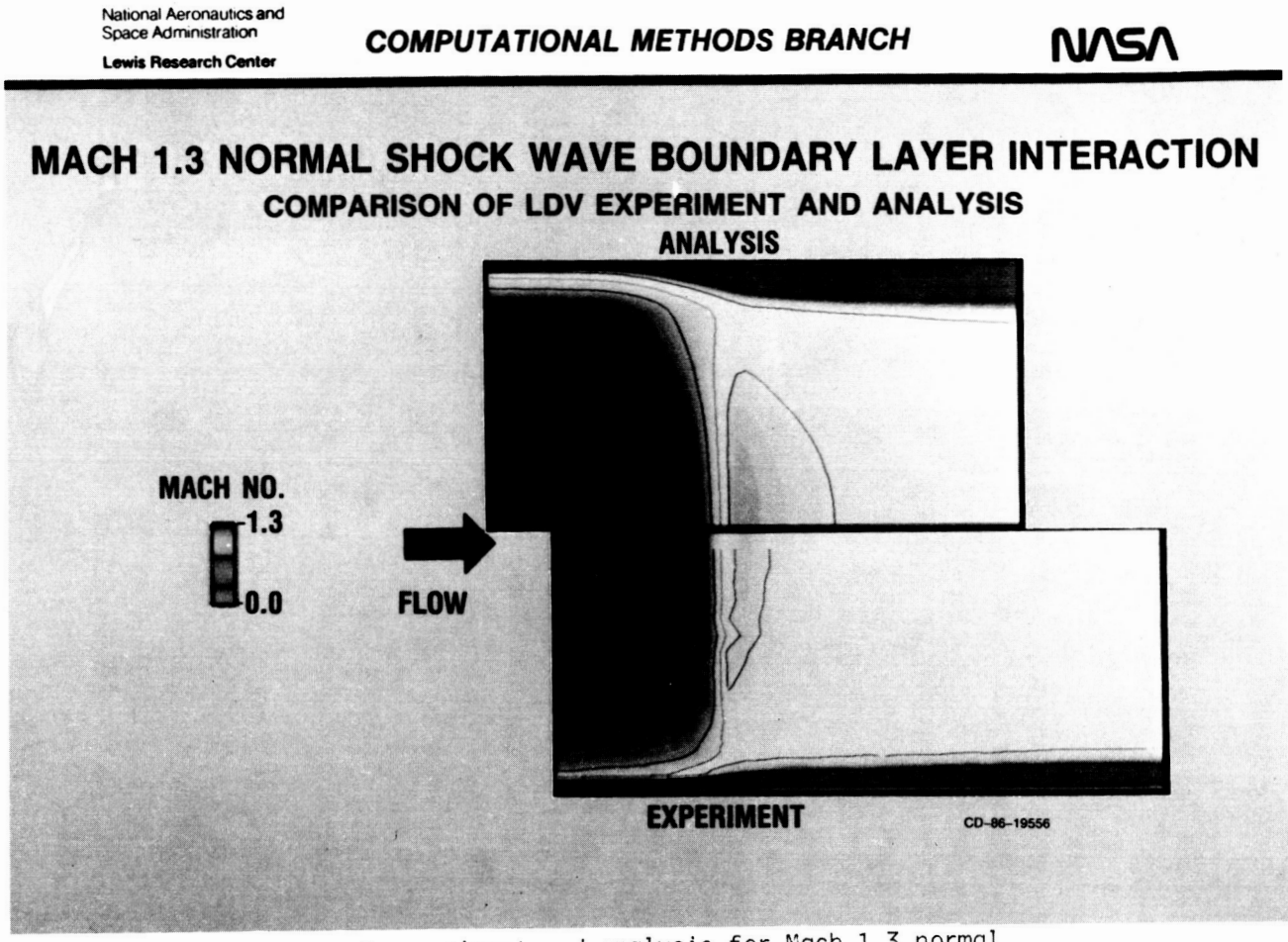

Figure 11. Comparison of experiment and analysis for Mach 1.3 normal shock boundary layer interaction

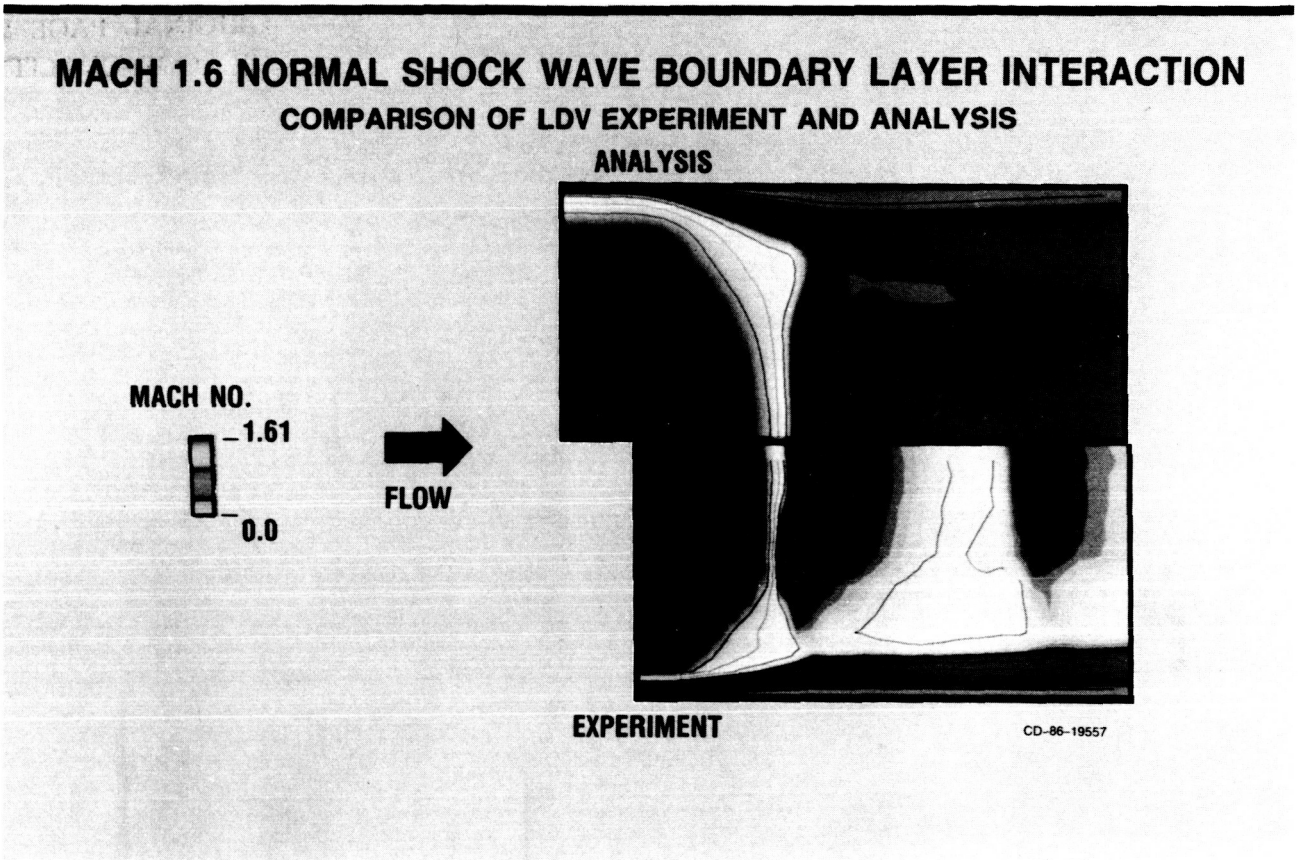

Figure 12. Comparison of experiment and analysis for Mach 1.6 normal shock boundary layer interaction

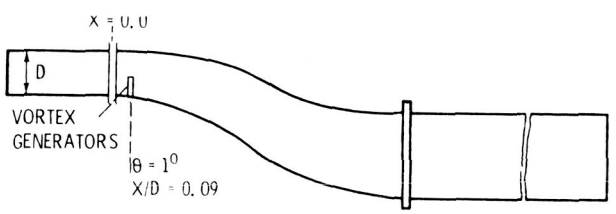

Figure 13.- Schematic of diffusing S-duct showing the axial location of the vortex generators.

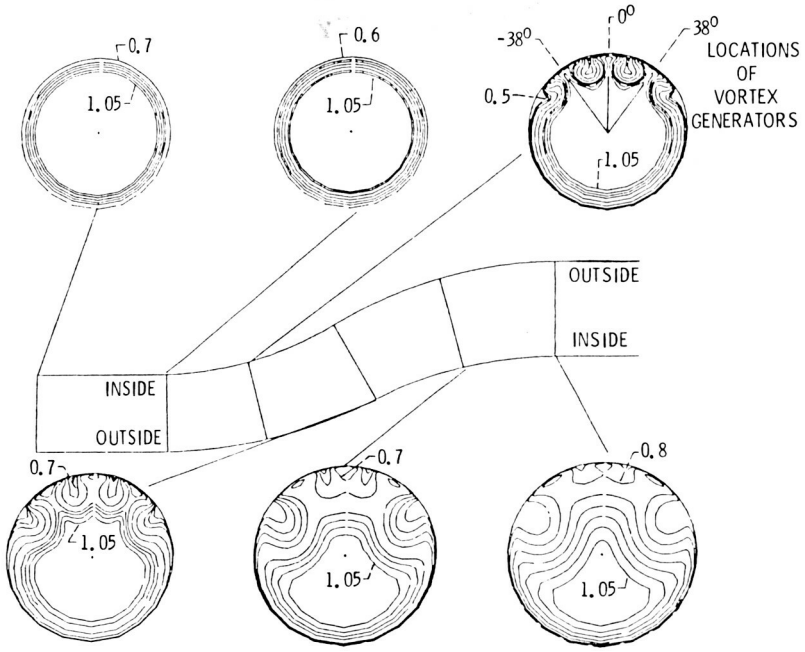

(a) Computed total pressure coefficient contours for S-duct with v. g.'s.

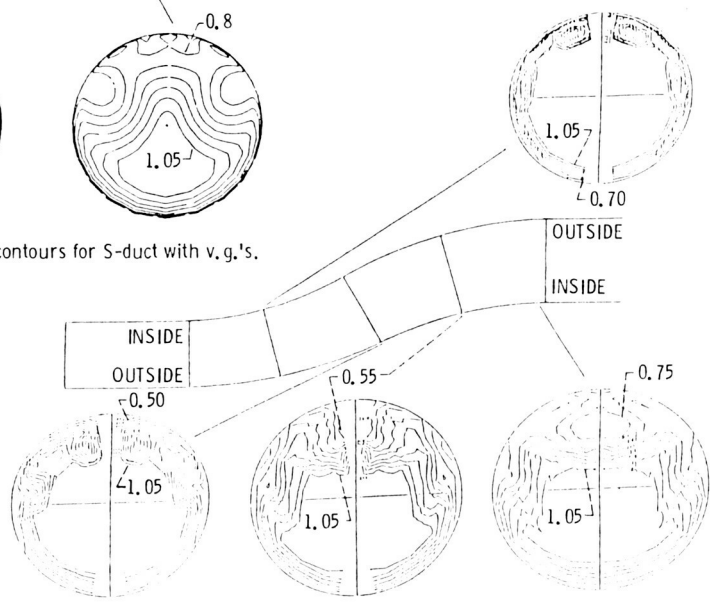

(b) Experimental total pressure coefficient contours for S-duct with v. g.'s.

Figure 14.

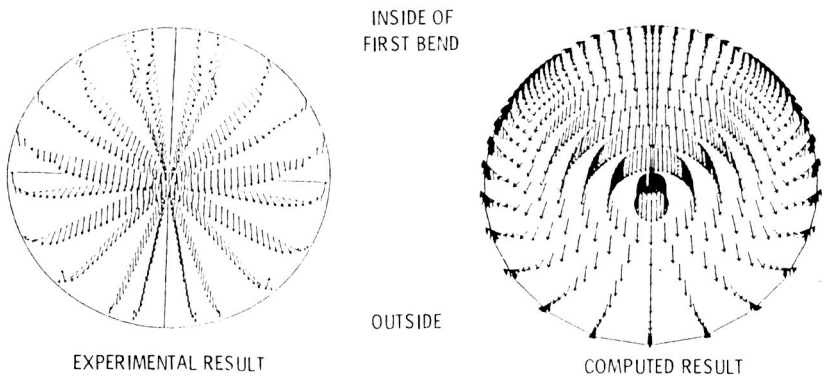

Figure 15. - Comparison of secondary flow at the inflection plane for S-duct with v. g.'s.